Evolution of Local Structural Motifs in Colloidal Quantum Dot Semiconductor Nanocrystals Leading to Nanofaceting

Bo Hou, Felix Cosmin Mocanu, Yuljae Cho, Jongchul Lim, Jiangtao Feng, Jingchao Zhang, John Hong, Sangyeon Pak, Jong Bae Park, Young-Woo Lee, et al.

Evolution of Local Structural Motifs in Colloidal Quantum Dot Semiconductor Nanocrystals Leading to Nanofaceting

Bo Hou[*,a,§], Felix Cosmin Mocanu[*,b,§], Yuljae Cho[c,d], Jongchul Lim[e], Jiangtao Feng[f], Jingchao Zhang[g], John Hong[c,h], Sangyeon Pak[c,i], Jong Bae Park[c], Young-Woo Lee[c], Juwon Lee[c], Byung-Sung Kim[c], Stephen M. Morris[c], Jung Inn Sohn[j,*], SeungNam Cha[k,*] and Jong Min Kim[l]

[a]School of Physics and Astronomy, Cardiff University, Queen's Building, The Parade, Wales, CF24 3AA, United Kingdom. Email: Houb6@cardiff.ac.uk

[b]Laboratoire de Physique de l'École Normale Supérieure, ENS, Université PSL, CNRS, Sorbonne Université, Université de Paris, 75005 Paris, France. Email: felix-cosmin.mocanu@phys.ens.fr

[c]Department of Engineering Science, University of Oxford, Parks Road, Oxford OX1 3PJ, United Kingdom.

[d]University of Michigan–Shanghai Jiao Tong University Joint Institute, Shanghai Jiao Tong University, 800 Dong Chuan Road, Minghang District, Shanghai 200240, China.

[e]Graduate school of energy science and technology, Chungnam National University, Daejeon, 34134, Republic of Korea.

[f]Department of Environmental Science & Engineering, School of Energy and Power Engineering, Xi'an Jiaotong University, Xi'an, 710049, China.

[g]Microsoft Corporation, Redmond, WA 98052, USA

[h]School of Materials Science and Engineering, Kookmin University, Seoul 02707, Republic of Korea

[i]School of Electronic and Electrical Engineering, Hongik University, Seoul 04066, Republic of Korea

[j]Division of Physics and Semiconductor Science, Dongguk University-Seoul, Seoul 04620, Republic of Korea. Email: junginn.sohn@dongguk.edu

[k]Department of Physics, Sungkyunkwan University, Suwon, Gyeonggi-do 16419, Republic of Korea. Email: chasn@skku.edu

[l]Department of Engineering, Electrical Engineering Division, 9 JJ Thomson Avenue, University of Cambridge, Cambridge, CB3 0FA, United Kingdom

§ B. H. and F. C. M. contributed equally to the work.

Abstract

Colloidal nanocrystals (NCs) have shown remarkable promise for optoelectronics, energy harvesting, photonics and biomedical imaging. In addition to optimising quantum confinement, the current challenge is to obtain a better understanding of the critical processing steps and their influence on the evolution of structural motifs. Computational simulations and electron microscopy presented in this work show that nanofaceting can occur during nanocrystal synthesis from a Pb-poor environment in a polar solvent. This could explain the curved interfaces and the olive-like shaped NCs observed experimentally when these conditions are employed. Furthermore, the wettability of the PbS NCs solid film can be further modified via stoichiometry control, which impacts the interface band bending and, therefore, technologies such as multiple junction deposition and interparticle epitaxial growth. Our results suggest that nanofaceting in NCs can become an inherent advantage when used to modulate band structures beyond what is traditionally possible in bulk crystals.

Keywords: Quantum Dots, Morphology, Electron Microscopy, Density functional theory

Compared to conventional semiconductor manufacturing approaches, solution-processed compound semiconductors combine cost-effective processing, scalable fabrication and compatibility with flexible substrates, which suggests that they are promising building blocks for next-generation semiconductor technologies.[1,2] Much progress has been made towards the goal of solution-processed solid films based on multi-layer deposition processing and heteroepitaxial growth in the area of colloidal semiconductors technologies, such as the recently commercialised passive-mode photoluminescence colloidal quantum dot semiconductor nanocrystals (NCs) display and lighting products.[3,4] However, the performance of the corresponding active-mode devices such as electroluminescence, field effect transistors and photovoltaic devices needs further improvement to meet the stringent requirement of industrial applications. The limited understanding of NCs processing parameters affecting active-mode device performance, remains a challenge in developing further advanced solution processable technologies.[4,5]

Due to the large surface area to volume ratios and solution-processability of NCs, stoichiometry and solvent effects are considered to be the key internal and external parameters, respectively, that define the unique physicochemical properties of the NCs. To complement the quantum confinement band gap engineering, one can manipulate the electronic and crystal structure properties of NCs by changing the surface bonding states, the solvent, and the overall composition.[7, 8] Carrier mobility can be affected by changing the inter-particle dielectric environment and the charge transfer distance.[9] On the other hand, through appropriate surface states and stoichiometry, one can also modulate the electronic trap sites, alter carrier/exciton lifetimes and even improve the solubility of NCs.[2, 7]

Surface ligands are one of the commonly used stabilisers for preventing oxidation of the NCs surfaces and reducing the agglomeration of nanoparticles.[10] In particular, mediated by either a polar or nonpolar solvent, the cascaded surface capping ligand exchange can result in atomic-

resolution deposition of multiple layers of NCs to form solid films. This process has attracted significant attention in colloidal epitaxial growth for optoelectronic devices.[11-16] Thus, rationally selected ligands can exchange the 'native' ligands through their electrostatic or nucleophilic interactions toward the NCs, this can provide lattice anchoring sites for new layers of NCs during the deposition process.[17,18] However, the understanding of the fundamental evolution process of the structural motifs from these nanoscale building blocks is still unclear and the primary steps and mechanism that determines the NCs solvent wettability and variation in the band structure for different solvents and stoichiometry have been barely explored to date.[19]

Herein, based on density function theory (DFT) models and electron microscopy studies of a typical rock-salt cubic binary lead sulphide (PbS) model, we reveal that the nanofaceting process is the key step that underpins stoichiometry and solvent effects on the modulation of the surface energy and morphology of individual NCs. The nanofaceting process enables the evolution of local structural motifs, which reflects the changes in their physicochemical and optical-electronic properties. The DFT calculation of the surface energies enables the prediction of the thermodynamically stable morphology. In order to predict the NCs shape, the NCs surface energy was minimized using a Wulff construction,[20] as implemented in Wulffpack.[21] We have taken into consideration not only the low-index {100}, {111} and {110} facets but also higher-index surfaces such as the {311} family, that are observed infrequently. The low-index non-polar {100} family of surfaces is the most stable one in vacuum and results in a near-cubic morphology for the nanocrystal. When solvent polarity is taken into account polar surfaces become more stable relative to non-polar ones, and the shape of the nanocrystal changes from a cube to a truncated octahedron.

Table 1. Calculated surface energies in (meVÅ^{-2}). Polar surfaces are labelled by their termination (Pb or S) and the (2x1) reconstructions are included in the case of (111) surfaces.

Surface index	Pb-rich			Pb-poor		
	vacuum	ODE	methanol	vacuum	ODE	methanol
(100)	23.7	36.2	34.6	23.7	36.2	34.6
(110)	35.4	35.2	32.1	35.4	35.2	32.1
$(111)_{Pb}$	63	63.2	62.9	98.3	98.8	98.5
$(111)_{S}$	83.4	83.8	83.5	50.4	51	50.6
$(111)_{Pb}$ (2x1)	28.4	28.5	25.8	28.4	28.5	25.8
$(111)_{S}$ (2x1)	33.8	33.6	30.5	33.8	33.6	30.5
$(311)_{Pb}$	30.5	30.8	30	45	45.2	44.5
$(311)_{S}$	43.6	43.9	42	29.1	29.4	27.5

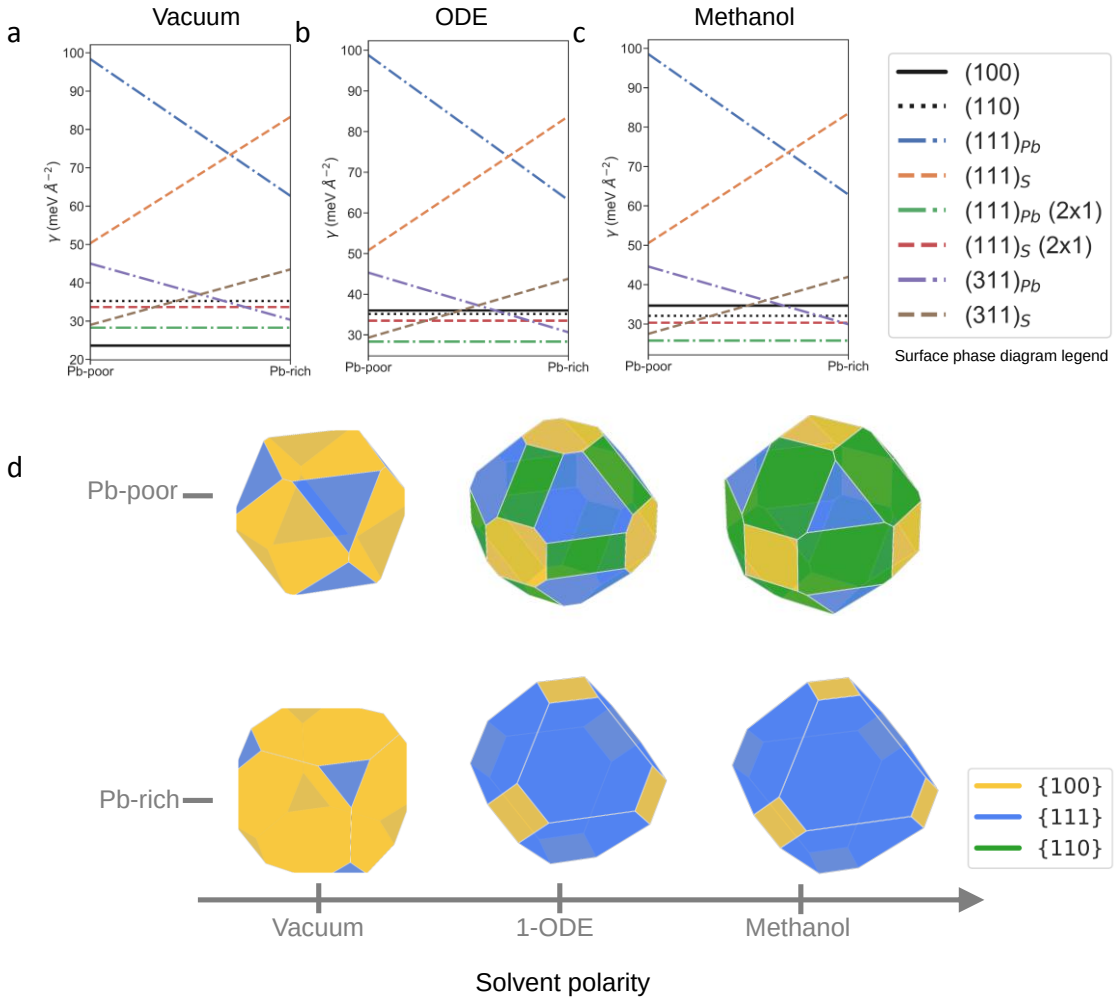

Figure 1. Surface phase-diagram and corresponding surfaces legends of PbS NCs in (a) vacuum, (b) 1-octadecene (ODE) and (c) Methanol. (d) The corresponding Wulff

constructions of PbS NCs as a function of stoichiometry and solvent polarity. {100} facets are shown in yellow, {111} facets are shown in blue and {110} facets are shown in green.

Once the surface energies have been calculated we produce a surface phase-diagram which is shown in Table 1 and Figure 1. The non-polar {100} surface is shown as a solid black line while the non-polar {110} surface is shown as a dotted line. We have considered both terminations of the {111} polar surface: the surface energy of the Pb-terminated facets is shown as a blue dashed-dotted line and an orange dashed line is used for the S-terminated facet. The (2x1) reconstructions ("Wood notation") of the corresponding {111} surfaces are shown as green dash-dotted lines (Pb- terminated) and red dashed lines (S-terminated). Similarly, {311} polar surfaces are shown as purple dashed-dotted lines (Pb-terminated) and brown dotted lines (S-terminated), respectively.

In vacuum, surface energies are dominated by the non-polar {100} facets and the appearance of polar {111} facets, which is similar to previous studies.[22] In order to capture the solvent effects, we have used an implicit solvation model as implemented in the VASPsol package.[22,23] When solvent screening is in taken into account (Figure 1b and Figure 1c), the energy of the non-polar facets increases whereas that of the polar facets decreases. These effects increase with the solvent polarity which validates the materials and device processing protocols that are normally used.[24]

Figure 1d shows detailed local motif variation as a function of stoichiometry. The non-polar {100} family of surfaces is the most stable one in vacuum which results in a near-cubic morphology for the nanocrystal (Figure 1). In vacuum and Pb-poor conditions, the preferred shape is close to a cube and Pb-rich conditions result in an increased area of {111} (Pb-terminated) facets. When solvent screening is taken into account (ODE and Methanol), the faceting becomes more pronounced. In particular, Pb-rich conditions now result in a

truncated octahedron nanocrystal shape that is dominated by {111} (Pb-terminated) facets while Pb-poor nanocrystal models display significant {110} facets that play a role in the experimentally observed self-assembly which will be further discussed in the microscopy and diffraction analysis.

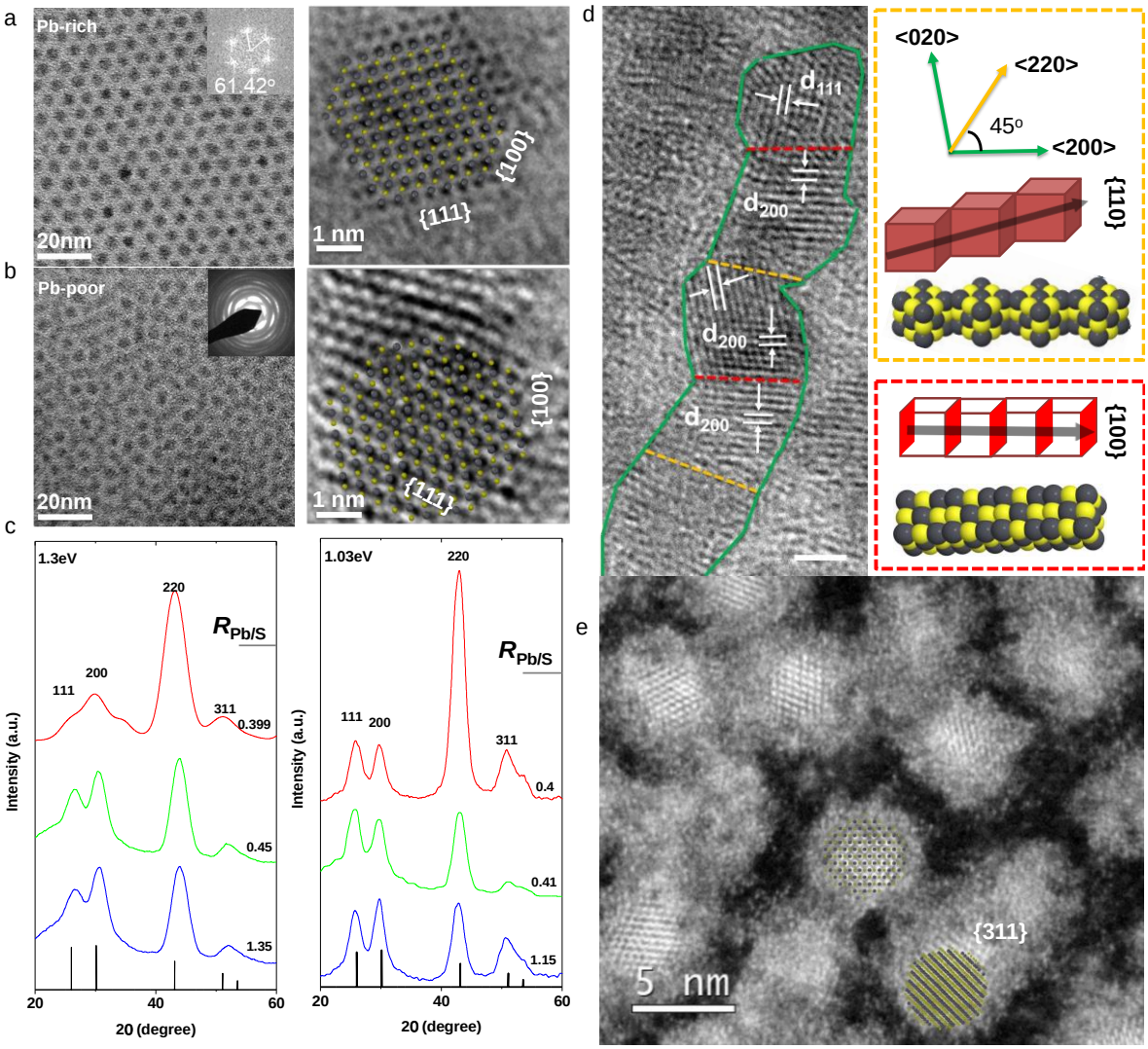

Figure 2 a, b) TEM (left) and HRTEM (right, view down from [011] zone axis) images of 1.3 eV oleic acid (OA) capped PbS NCs (PbS@OA) film with Pb-rich (Pb:S=1.35) and S-rich (Pb:S=0.39) configuration. Inset images highlight the *hcp* particle packing sequence through generating FFT and the corresponding SAED patterns of the texture structure. HRTEM {100} and {111} cross-grating patterns are also highlighted. c) XRD patterns of 1.3 eV and 1.03 eV band gap PbS NCs samples with different Pb/S ratio. d) HRTEM image of S-rich PbS NCs (Pb/S=0.39). The lattice spacing and bridging orientation were indexed as highlighted in the image and scale bar equal to 1 nm. e) High-resolution HAADF-STEM images of PbS NCs (Pb/S=0.39) after methanol washing.

We prepared different stoichiometric PbS NCs in ODE according to our previous works with slightly modification (Supporting Information, SI, Table S1, SII, Figure S1, Table S2).[12, 25, 26] As shown in Figure 2a, the symmetrically ordered Pb-rich PbS NCs form a superstructure with a standard hexagonal close packing (*hcp*) arrangement. This is apparent from the transmission electron microscope (TEM) image and the corresponding Fast Fourier transform (FFT) pattern (e.g., intersection angle = $61.42^{o} \pm 1.54^{o}$). Nonetheless, this periodicity of the superstructure is absent for the S-rich PbS NCs (Figure 2b). Instead, a textured crystal structure with a high packing density is identified as shown in the selected area electron diffraction (SAED) pattern in Figure 2b (inset image). Powder X-ray diffraction (XRD) analysis (Figure 2c) and high-resolution TEM (HRTEM) analysis (Figure 2d) suggests that this textural crystal features arise from a [110] directional attachment, which breaks the symmetry of the NC arrangement.[27, 28]

The surface phase diagrams (Figure 1a, b and c) and Wulff constructions (Figure 1d) show that polar {311} facets can be very low in energy when solvent effects are taken into account. This corroborates previous observations of nanofaceting effects observed in PbSe nanocrystals.[29,30] The S-terminated {311} facets are also lower in energy in Pb-poor conditions when compared to their Pb-terminated counterparts in Pb-rich conditions. This in turn might explain the observed olive shape of PbS nanoparticles synthesised in Pb-poor conditions (HRTEM, Figure 2b) and in a polar solvent (methanol, Figure 2e) as nanofaceting will result in more curved interfaces. A Wulff construction (overlay of atomic models) including these high-index polar facets for a nanocrystal synthesised in Pb-poor conditions and a polar solvent (Methanol) is shown in the inset of Figure 2a, b and e (Pb atoms are shown in grey while S atoms are shown in yellow, see further details in HRTEM simulations in SII, Figure S2-S3). Alternatively, the elongated particles obtained in Pb-poor conditions (Figure 2d) could be the result of {110} faceting, the formation of dimers and the resulting

reorganization of the nanocrystal which was also previously reported experimentally and studied theoretically.[28, 31,32] It is worth mentioning that {311} facets have been found to be quite rare in the microscopy results (Figure 2e) but they can be difficult to resolve, and to differentiate experimentally from the other facets, in particular the {111} facets.

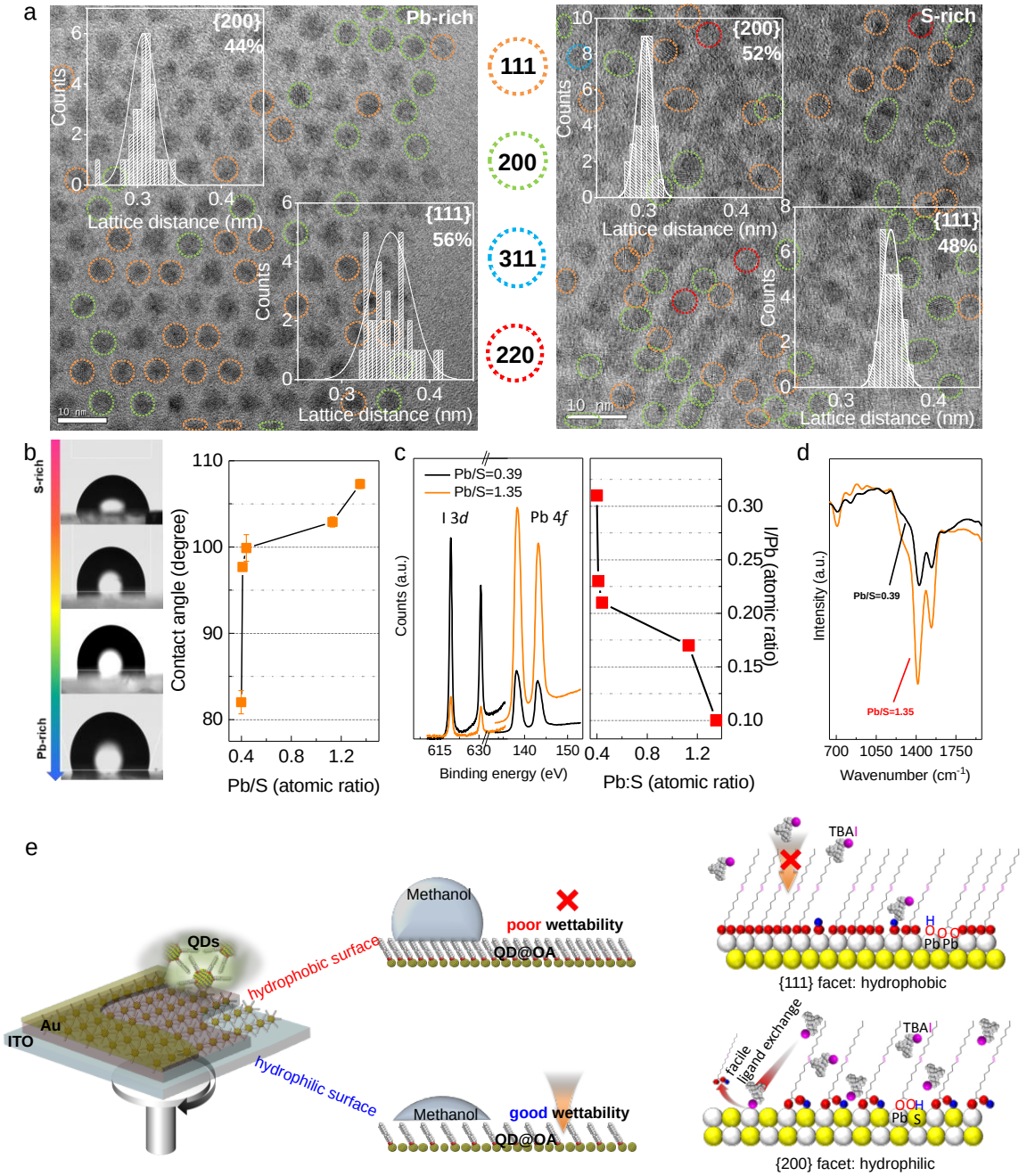

Figure 3. a) HRTEM images and statistical analysis results (inset) of as-prepared 1.3 eV band gap PbS NCs with Pb/S ratio of 1.35 (left) and 0.39 (right). b) The contact angle of 1.3 eV band gap PbS@OA NCs with different stoichiometry. c) XPS spectra (left panel)

produced from TBAI treated off-stoichiometric PbS NCs with Pb/S ratio equal to 0.39 (black curve) and 1.35 (red curve) respectively. The I/Pb atomic ratio as a function of the Pb/S ratio is shown in the right panel. d) Magnified FTIR spectrum of oleic acid-capped different stoichiometry PbS NCs. e) A schematic illustration of the NCs solid-state ligand exchange process (left panel). The right panel shows the surface bonding configurations of PbS@OA NCs.

Interestingly, through statistical analysis of HRTEM images (Figure 3a), we found that the Pb-rich NCs (synthesized in ODE) are mainly terminated by {111} planes ({111} population=56%). However, when we enriched the amount of sulphur in the PbS NCs (synthesized in ODE), the ratio of {200} planes dramatically increased and made the ratio between the {111} and {200} facets change from 8:6 to 8:9 ({200} population=53%). Because the carboxyl moiety preferentially binds to the Pb atom, changing the local facet motif of NCs will inevitably affect the population of the surface bonding states and the surface polarity.[33, 34] For all measurements we have used a cryostat holder to minimize beam damage and reduce the possibility of reorientation, though we cannot completely exclude that NC may reorient under the electron beam.

As expected, we found that the Pb/S ratio can control the wettability of the PbS@OA films. We show in Figure 3b, that the contact angle of the 1.3 eV band gap Pb-rich PbS@OA film is 107.3 ± 4.81°, which is much larger ($\Delta \sim 25°$) than the S-rich PbS@OA film (82.01 ± 2.91°). The solid phase with good wettability can induce a larger volume of the liquid to disperse into the grain boundaries, and it can subsequently enhance ligand exchange efficiency.[35, 36] A methanol dispersed TBAI ligand solution was selected to replace the long-chain aliphatic ligands on the NCs surface in order to investigate the variation of wettability (PbS@TBAI, SI).[25, 26, 37, 38] The smaller the contact angle is, the better the wettability of the hydrophilic ligand solution (i.e., Methanol + TBAI).[35] Indeed, quantized X-ray photoelectron spectroscopy (XPS) analysis reveals that, after TBAI ligand exchange, the S-rich NCs film

has more iodine (I) intercalation compared to the Pb-rich NCs (Figure 3c). This indicates that an S-rich PbS@OA films can provide a favourable wetting as iodide ions are able to replace more of the carboxyl moieties from PbS NCs surface. An important difference between the Pb-rich and Pb-poor NC assemblies is that the Pb-rich conditions favour a more ordered packing arrangement, while Pb-poor conditions result in a disordered assembly of particles. However, for 3D stacking multiple layers QD films, the QD assemblies seems to be random ordered, which may be due to non-equilibrium dynamical spin-coating and ligand exchange process (Figure S4).

In Figure 3d, for the under same film thickness (SII, Figure S5, Table S3), FTIR and nuclear magnetic resonance (NMR, Figure S6-S7) analysis reveal that Pb-rich PbS NCs films have more surface OA compared to an S-rich film. This surface deficiency of OA ligands is due to the lack of Pb-terminated sites on the S-rich NCs.[34] This bonding state variation can subsequently affect the NCs packing arrangement.[11] We believe that the augmented population of {200} planes not only leads to the attachment along the {110} direction of the NCs assembly and to the shape changing (e.g., ellipsoidal shape Figure 2b) but it also affects the surface bonding configuration from of the as-prepared PbS@OA films.[27, 34] Based on theoretical calculations, the binding energy of OA on a PbS NC surface is different between the {111} and {200} planes.[11, 34]

As exemplified in Figure 3e, the deprotonated OA and hydroxide moieties are identified to be coordinate bonded on the {111} planes which are difficult to eliminate during the solid-state ligand exchange process.[34, 39, 40] However, in the case of the {200} planes, the OA was determined to be weakly adsorbed on their surface, which can be easily removed by applying an acidic ligand solution (e.g., methanol+TBAI).[11, 26, 39, 40] Therefore, through deliberately enriching the populations of the {200} planes (i.e., S-rich NCs), we can manipulate the surface wettability of the PbS@OA NCs and hence enhance the inorganic (i.e., NCs) and

organic (i.e. ligands) interface reaction for improving NC film ligand exchange efficiency and potentially colloidal epitaxy-growth.

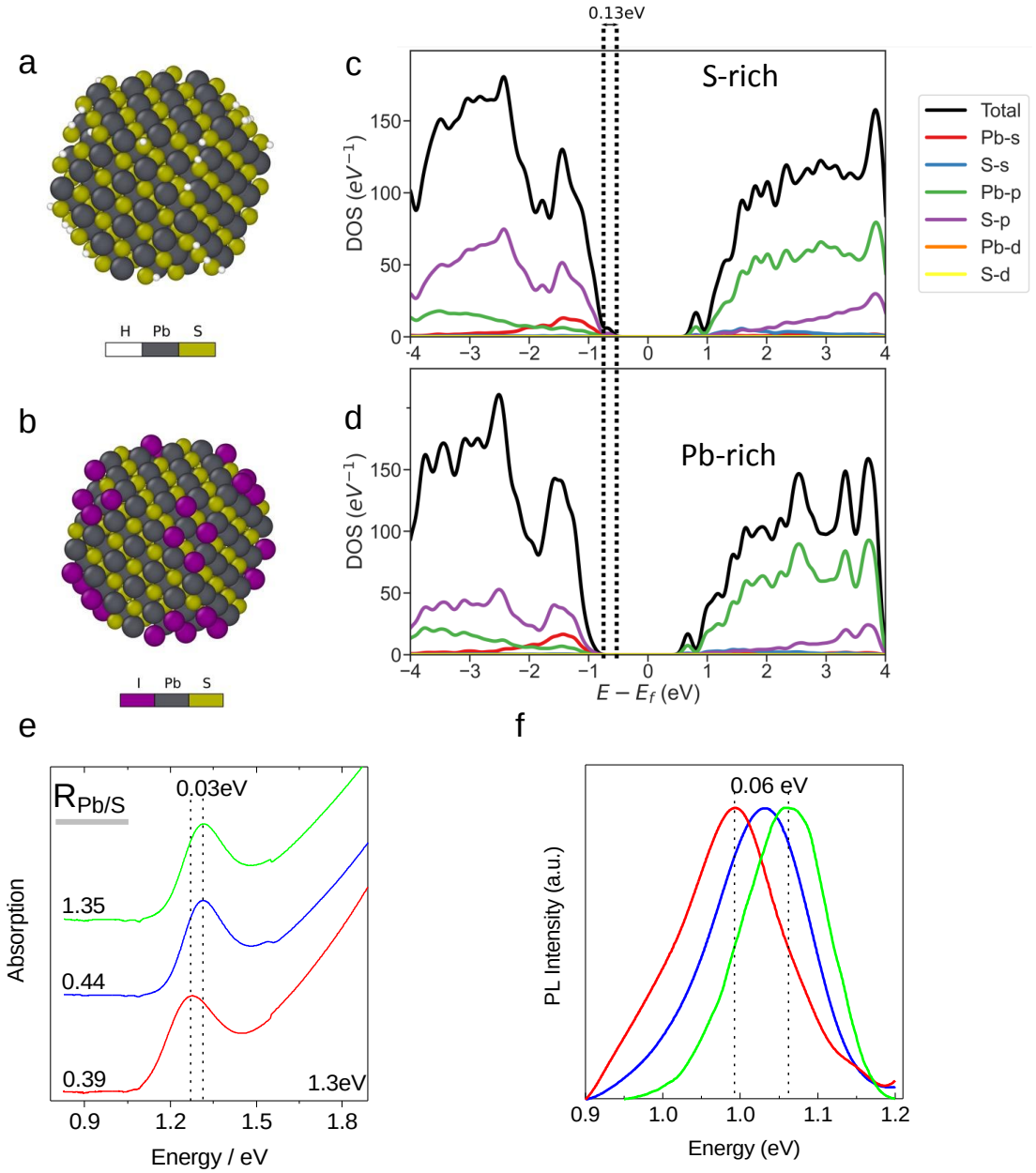

Figure 4. Visualization of a passivated nanocrystal for a PbS NC in S-rich a) and Pb-rich b) conditions. Partial density of electronic states of a passivated nanocrystal for a PbS NC in S-rich c) and Pb-rich d) conditions. Pb atoms are shown in grey, S atoms are shown in yellow, Hydrogen (H)-atoms are shown in white, and I atoms are shown in purple. Absorption

spectroscopy e) and photoluminescence f) analysis results for typical 1.3 eV bandgap PbS NCs solution in different Pb/S ratio. As highlighted in the figures, the peak position offset is around 0.03 eV (absorption) and 0.06 eV (PL), respectively.

The NC models for the Pb-rich and Pb-poor NCs of ~ 2.4 nm in diameter were generated using the Wulff construction shapes previously obtained and shown in Figure 1. Both NCs models are close to a 1:1 Pb:S ratio and have a similar cubic shape, exposing either Pb-terminated or S-terminated polar {111} facets, as shown in Figure 4a and 4b. In order to passivate these polar facets, counter-ion ligands were added, namely I atoms were placed on the Pb-terminated {111} facets, following previous work.[41] In the case of S-terminated {111} facets, H atoms were used in order to obtain passivation. The electronic structure of these nanocrystal models was evaluated and a partial density of states is shown in Figure 4c for the Pb-poor NC model and in Figure 4d for the Pb-rich NC model. Given the structural similarity of the two models, their partial electronic densities of state are also quite similar. In both cases the top of the valence band is dominated by S-p and Pb-s states while the bottom of the conduction band is dominated by Pb-p states. It is known that DFT calculations can significantly underestimate the band gap.[42] In order to correct for this, we have used the GLLB-SC calculation including the derivative discontinuity.[43] The DFT calculation finds that the Pb-poor NC has a bandgap of 1.471 eV compared to 1.604 eV for the Pb-rich. Rather than the absolute values we focus on the reduction of the band gap (0.13 eV) in Pb-poor conditions, which appears to be caused by the changes in the valence band of the material due to the stoichiometric excess of S. The absolute values of the band gaps of both models are slightly larger than those observed experimentally but are reasonable given the model size (~2.4 nm) and the approximations made. Most importantly, the DFT estimation including the derivative discontinuity of the Kohn-Sham potential is able to reasonably capture the magnitude of the band gap reduction in Pb-poor conditions that was observed experimentally (Figure 4e and Figure 4f). As shown in Figure 4e and 4f, red-shifted exciton absorption (0.03

eV) and PLs (0.06 eV) were observed. The band gap reduction trend from the Pb-rich to S-rich correlates well also with the increased packing densities as observed in Figure 2.[9, 44]

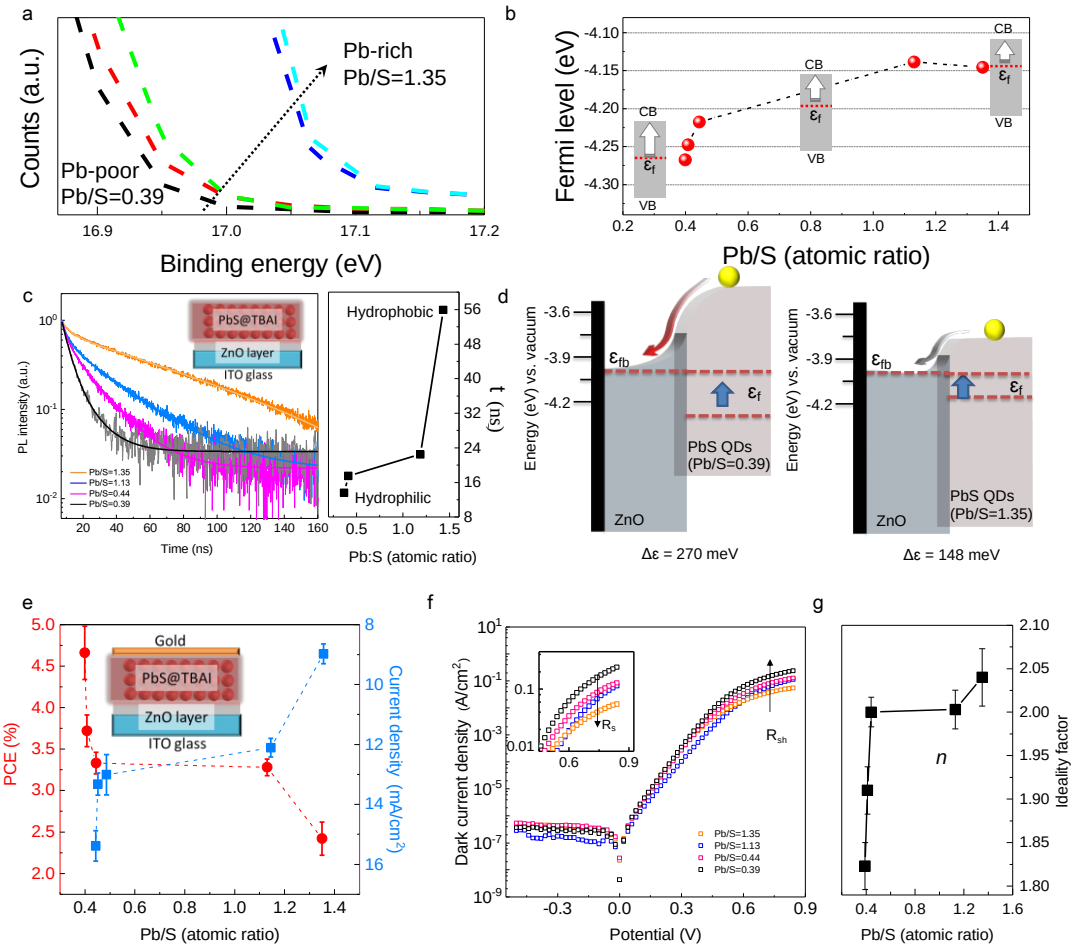

Figure 5. a) The magnified spectra near the secondary electron cut-off region of the UPS spectra for PbS@TBAI NCs films with different Pb/S ratio. b) The identified binding energy values (i.e., Fermi levels) as a function of the Pb/S ratio. c) TRPL of the PbS@TBAI NCs films with different element ratios. Inset image shows a cross-section of the device configuration. d) The band alignment schematics of the ZnO films (ε_{fb}=-4.00 related to 1.3 eV PbS@TBAI in the equilibrium state. The energy levels at the open circuit condition are also provided (red dashed line). Valence band edges of the ZnO scheme are not drawn to scale. e) PCE (red legend) and Jsc (blue legend) values evolution as a function of the NCs Pb/S ratio. The error bars were generated from standard deviation across nine samples on three different substrates. Inset image shows a cross-section of the photovoltaic device configuration f) Semi-logarithm J–V curves for the dark diode analysis. g) Calculated ideality factor values (n) for different Pb/S ratios. Arrows indicate the increasing direction of R_s and R_{sh}.

The variation of the Pb/S ratio can also effectively modulate the Fermi levels and density of states (DOS) in the as-prepared PbS NCs film which were identified to originate from the charge carrier density alternations.[8] The variation in the binding energies from different wettability PbS NC (e.g., band gap equal to 1.3 eV) was exemplified from ultraviolet photoelectron spectroscopy analysis (UPS, Figure 5a and Figure S8).[12] As summarised in Figure 5b, when the NC are Pb-rich (hydrophobic), the electron concentration increases and the Fermi level shifts toward the conduction band (CB). As the NC becomes S-rich (hydrophilic), the hole concentration increases and the Fermi level drops toward the intrinsic mid-band gap level. It should mention that a DOS variation (e.g., band edge shifting) with the enrichment of either S or Pb content was also observed from our UPS analysis (Figure S8) which is consistent with previous DFT simulation results.[7, 13, 27, 28, 33, 40] This ca. 0.17 eV DOS variation can be attributed to the cation or anion adsorption/desorption on the surface of NC which changes the strength of the NC-ligand surface dipole and chemical electronegativity.[7, 40]

As shown in Figure 5c, the hydrophilic NCs films also display a much shorter PL decay in the time-resolved photoluminescence (TRPL) measurement. For the PL measurement, we employed a ZnO quenching layer which is the typical electron transport layers in PbS NC based diode junction devices (Figure 5c, inset). The dynamics of the exciton is complex as it includes charge transfer and transport within the ZnO interfaces because the presence of the ZnO layer facilitates carrier extraction, which adds another nonradiative pathway that competes with radiative and trap-assisted recombination.[45,46] To quantify and compare the photogenerated charge carrier lifetimes, we fit the TRPL decay with a stretched exponential model to obtain lifetime.[47] The use of this model has been previously suggested to take into account a distribution of monomolecular (e.g., exponential decay) and bimolecular

recombination (e.g., biexponential decay) processes which provide a proper way to rationalising complicated exciton dynamics.[47-49] As shown in Figure 5c, the mean lifetime of charge carrier reduced from 55.93 ± 0.33 ns to 13.65 ± 0.39 ns as the NCs modified from being hydrophobic to hydrophilic. A shorter lifetime and decreased PL intensity are indicators of the exciton dissociation having been effectively enhanced.[47] It prove that the hydrophilic PbS@TBAI NCs can lead to an efficient charge transfer to ZnO NCs producing a charge-separated state which decays non-radiatively.[45,46] In Figure 5d, two types of Fermi level (ε_f) alignment between the flat band potential (ε_{fb}) of ZnO and PbS@TBAI are exhibited. In the open circuit condition, the Fermi level is offset between the ZnO and S-rich or Pb-rich PbS NCs were 270 meV and 148 meV respectively.

The improved ligand exchange reaction and a steep band bending are beneficial to exciton dissociation and charge collection.[50,51] The as-prepared NC solar cell (NCSC) power conversion efficiency (PCE) shows enhancement unambiguously due to the S-enrichment. The solar cell structure was similar to our TRPL measurement which employed TBAI as the only ligand (Figure 5c inset, 12 layers of NC@TBAI in total, Figure S5, Table S3) and gold as the anode. As rationalised in Figure 5e, the NCSC PCE performance can be improved more than two times when the NC are altered from being hydrophobic (PCE~2%) to hydrophilic (PCE~5%). The J_{sc} values of the NCSC can be enhanced from 8.98 ± 0.82 mA/cm^2 to 15.39 ± 0.80 mA/cm^2, which are resulted from the improved ligand exchange efficiency and the enlarged band bending (Figure S9). Figure 5f and Figure 5g show the semi-log dark current J-V curves and ideality factor (*n*) as a function of the Pb/S ratio. Benefitting from the large band bending from the S-rich NCs, the charge carrier pathways are largely suppressed under forward bias which reflects the larger shunt resistance (R_{sh}) as indicated in Figure 5f. On the other hand, the enhanced ligand exchange efficiency also

promotes the reduction of Ohmic losses from the series resistance (R_s). The IR drops and minimises recombination, tunnelling, and inhomogeneity at the junction interface (i.e., decreasing the leakage currents).[52] Furthermore, the *n* values were estimated by correlating results from both fitting the simple diode equation (Equation 1)[53, 54] and solving the diode equation through conductance derivative methods (Equation 2).[55] In Figure 5g, the *n* values are reduced from 2.04 to 1.82 by enriching the S components in the PbS NCs (Figure S10-S12, and Table S4-S6), which indicates that the charge recombination across the junction was sufficiently reduced.[38, 55, 56]

$$\begin{cases} \ln I = \ln I_0 + \frac{\mathrm{qV}}{\mathrm{n}k_B T} \text{ (Equation 1)} \\ \frac{\partial V}{\partial \ln I_{cor}} = \frac{n}{\beta} + R_s I_{cor} \text{ (Equation 2)} \end{cases}$$

In conclusion, our findings indicate that stoichiometric and solvent control can be used in tandem to stabilise polar surfaces. This nanofaceting process determines the solution-processed NC morphology and the change in optoelectronic properties of devices. The simulation framework deployed here could be further extended to study the stability of nanocrystals further away from a Pb:S ratio of 1:1, as well as the effects of ligand exchange, and work is underway on these topics. Moreover, we believe the nanofaceting is not only limited to PbS NC, but it can also apply to other compound semiconductors such as ternary metal chalcogenide, metal phosphide and perovskite metal halides.

Supporting information

Includes information of QDs and device preparations (SI, Table S1), DFT calculations (SI), composition analysis (Figure S1, Table S2, SII), film structure analysis, electron microscopies simulations (HRTEM, FIB, HAADF-STEM, Figure S2-S4, AFM, DekTak, Figure S5, Table S3), surface chemistry analysis (FTIR, Figure S6 and NMR, Scheme 1,

Figure S7), band structure analysis (UPS, Figure S8) and XPS and optical property analysis methods (UV-VIS-NIR and TRPL, SII), device characterization (Figure S9-S12, Table S4-S6, SIII).

Reference

(1) Kagan, C. R.; Lifshitz, E.; Sargent, E. H.; Talapin, D. V. Building devices from colloidal quantum dots. Science 2016, 353 (6302), aac5523.

(2) Yang, Y.; Qin, H.; Peng, X. Intramolecular Entropy and Size-Dependent Solution Properties of Nanocrystal–Ligands Complexes. Nano Letters 2016, 16 (4), 2127-2132.

(3) Li, B.; Lu, M.; Feng, J.; Zhang, J.; Smowton, P. M.; Sohn, J. I.; Park, I.-K.; Zhong, H.; Hou, B. Colloidal quantum dot hybrids: an emerging class of materials for ambient lighting. Journal of Materials Chemistry C 2020, 8 (31), 10676-10695.

(4) Osypiw, A. R. C.; Lee, S.; Jung, S.-M.; Leoni, S.; Smowton, P. M.; Hou, B.; Kim, J. M.; Amaratunga, G. A. J. Solution-processed colloidal quantum dots for light emission. Materials Advances 2022, 3, 6773-6790.

(5) Liu, M.; Yazdani, N.; Yarema, M.; Jansen, M.; Wood, V.; Sargent, E. H. Colloidal quantum dot electronics. Nature Electronics 2021, 4 (8), 548-558.

(6) Hou, B. Colloidal Quantum Dots: The Artificial Building Blocks for New-Generation Photo-Electronics and Photochemistry. Israel Journal of Chemistry 2019, 59 (8), 637-638.

(7) Brown, P. R.; Kim, D.; Lunt, R. R.; Zhao, N.; Bawendi, M. G.; Grossman, J. C.; Bulović, V. Energy Level Modification in Lead Sulfide Quantum Dot Thin Films through Ligand Exchange. ACS Nano 2014, 8 (6), 5863-5872.

(8) Oh, S. J.; Berry, N. E.; Choi, J.-H.; Gaulding, E. A.; Paik, T.; Hong, S.-H.; Murray, C. B.; Kagan, C. R. Stoichiometric Control of Lead Chalcogenide Nanocrystal Solids to Enhance Their Electronic and Optoelectronic Device Performance. ACS Nano 2013, 7 (3), 2413-2421.

(9) Liu, Y.; Gibbs, M.; Puthussery, J.; Gaik, S.; Ihly, R.; Hillhouse, H. W.; Law, M. Dependence of Carrier Mobility on Nanocrystal Size and Ligand Length in PbSe Nanocrystal Solids. Nano Letters 2010, 10 (5), 1960-1969.

(10) Tang, J.; Kemp, K. W.; Hoogland, S.; Jeong, K. S.; Liu, H.; Levina, L.; Furukawa, M.; Wang, X.; Debnath, R.; Cha, D.; et al. Colloidal-quantum-dot photovoltaics using atomic-ligand passivation. Nature Materials 2011, 10 (10), 765-771.

(11) Boles, M. A.; Ling, D.; Hyeon, T.; Talapin, D. V. The surface science of nanocrystals. Nature Materials 2016, 15 (2), 141-153.

(12) Hou, B.; Cho, Y.; Kim, B. S.; Hong, J.; Park, J. B.; Ahn, S. J.; Sohn, J. I.; Cha, S.; Kim, J. M. Highly Monodispersed PbS Quantum Dots for Outstanding Cascaded-Junction Solar Cells. ACS Energy Letters 2016, 1 (4), 834-839.

(13) Ip, A. H.; Thon, S. M.; Hoogland, S.; Voznyy, O.; Zhitomirsky, D.; Debnath, R.; Levina, L.; Rollny, L. R.; Carey, G. H.; Fischer, A.; et al. Hybrid passivated colloidal quantum dot solids. Nature Nanotechnology 2012, 7 (9), 577-582.

(14) Lee, S.; Choi, M.-J.; Sharma, G.; Biondi, M.; Chen, B.; Baek, S.-W.; Najarian, A. M.; Vafaie, M.; Wicks, J.; Sagar, L. K.; et al. Orthogonal colloidal quantum dot inks enable efficient multilayer optoelectronic devices. Nature Communications 2020, 11 (1), 4814.

(15) Balazs, D. M.; Dirin, D. N.; Fang, H.-H.; Protesescu, L.; ten Brink, G. H.; Kooi, B. J.; Kovalenko, M. V.; Loi, M. A. Counterion-Mediated Ligand Exchange for PbS Colloidal Quantum Dot Superlattices. ACS Nano 2015, 9 (12), 11951-11959.

(16) Choi, M.-J.; García de Arquer, F. P.; Proppe, A. H.; Seifitokaldani, A.; Choi, J.; Kim, J.; Baek, S.-W.; Liu, M.; Sun, B.; Biondi, M.; et al. Cascade surface modification of colloidal quantum dot inks enables efficient bulk homojunction photovoltaics. Nature Communications 2020, 11 (1), 103.

(17) Sun, B.; Vafaie, M.; Levina, L.; Wei, M.; Dong, Y.; Gao, Y.; Kung, H. T.; Biondi, M.; Proppe, A. H.; Chen, B.; et al. Ligand-Assisted Reconstruction of Colloidal Quantum Dots Decreases Trap State Density. Nano Letters 2020, 20 (5), 3694-3702.

(18) Kirmani, A. R.; Walters, G.; Kim, T.; Sargent, E. H.; Amassian, A. Optimizing Solid-State Ligand Exchange for Colloidal Quantum Dot Optoelectronics: How Much Is Enough? ACS Applied Energy Materials 2020, 3 (6), 5385-5392.

(19) Xia, Y.; Chen, W.; Zhang, P.; Liu, S.; Wang, K.; Yang, X.; Tang, H.; Lian, L.; He, J.; Liu, X.; et al. Facet Control for Trap-State Suppression in Colloidal Quantum Dot Solids. Advanced Functional Materials 2020, 30 (22), 2000594.

(20) Wulff, G. XXV. Zur Frage der Geschwindigkeit des Wachsthums und der Auflösung der Krystallflächen. Zeitschrift für Kristallographie - Crystalline Materials 1901, 34 (1-6), 449-530.

(21) Rahm, J. M.; Erhart, P. WulffPack: A Python package for Wulff constructions. Journal of Open Source Software 2020, 5 (45), 1944.

(22) Deringer, V. L.; Dronskowski, R. Stabilities and Reconstructions of Clean PbS and PbSe Surfaces: DFT Results and the Role of Dispersion Forces. The Journal of Physical Chemistry C 2016, 120 (16), 8813-8820.

(23) Mathew, K.; Sundararaman, R.; Letchworth-Weaver, K.; Arias, T. A.; Hennig, R. G. Implicit solvation model for density-functional study of nanocrystal surfaces and reaction pathways. The Journal of Chemical Physics 2014, 140 (8), 084106.

(24) Mathew, K.; Kolluru, V. S. C.; Mula, S.; Steinmann, S. N.; Hennig, R. G. Implicit self-consistent electrolyte model in plane-wave density-functional theory. The Journal of Chemical Physics 2019, 151 (23), 234101.

(25) Hou, B.; Kim, B.-S.; Lee, H. K. H.; Cho, Y.; Giraud, P.; Liu, M.; Zhang, J.; Davies, M. L.; Durrant, J. R.; Tsoi, W. C.; et al. Multiphoton Absorption Stimulated Metal Chalcogenide Quantum Dot Solar Cells under Ambient and Concentrated Irradiance. Advanced Functional Materials 2020, 30 (39), 2004563.

(26) Hou, B.; Cho, Y.; Kim, B.-S.; Ahn, D.; Lee, S.; Park, J. B.; Lee, Y.-W.; Hong, J.; Im, H.; Morris, S. M.; et al. Red green blue emissive lead sulfide quantum dots: heterogeneous synthesis and applications. Journal of Materials Chemistry C 2017, 5 (15), 3692-3698,

(27) Kim, D.; Kim, D.-H.; Lee, J.-H.; Grossman, J. C. Impact of Stoichiometry on the Electronic Structure of PbS Quantum Dots. Physical Review Letters 2013, 110 (19), 196802.

(28) Bertolotti, F.; Dirin, D. N.; Ibáñez, M.; Krumeich, F.; Cervellino, A.; Frison, R.; Voznyy, O.; Sargent, E. H.; Kovalenko, M. V.; Guagliardi, A.; et al. Crystal symmetry breaking and vacancies in colloidal lead chalcogenide quantum dots. Nature Materials 2016, 15 (9), 987-994.

(29) Cho, K.-S.; Talapin, D. V.; Gaschler, W.; Murray, C. B. Designing PbSe Nanowires and Nanorings through Oriented Attachment of Nanoparticles. Journal of the American Chemical Society 2005, 127 (19), 7140-7147.

(30) Fang, C.; van Huis, M. A.; Vanmaekelbergh, D.; Zandbergen, H. W. Energetics of Polar and Nonpolar Facets of PbSe Nanocrystals from Theory and Experiment. ACS Nano 2010, 4 (1), 211-218.

(31) Cui, J.; Panfil, Y. E.; Koley, S.; Shamalia, D.; Waiskopf, N.; Remennik, S.; Popov, I.; Oded, M.; Banin, U. Colloidal quantum dot molecules manifesting quantum coupling at room temperature. Nature Communications 2019, 10 (1), 5401.

(32) Hou, B.; Sohn, M.; Lee, Y.-W.; Zhang, J.; Sohn, J. I.; Kim, H.; Cha, S.; Kim, J. M. Chemically encoded self-organized quantum chain supracrystals with exceptional charge and ion transport properties. Nano Energy 2019, 62, 764-771.

(33) Grisorio, R.; Debellis, D.; Suranna, G. P.; Gigli, G.; Giansante, C. The Dynamic Organic/Inorganic Interface of Colloidal PbS Quantum Dots. Angewandte Chemie International Edition 2016, 55 (23), 6628-6633.

(34) Zherebetskyy, D.; Scheele, M.; Zhang, Y.; Bronstein, N.; Thompson, C.; Britt, D.; Salmeron, M.; Alivisatos, P.; Wang, L.-W. Hydroxylation of the surface of PbS nanocrystals passivated with oleic acid. Science 2014, 344 (6190), 1380-1384.

(35) Tian, J.; Shen, T.; Liu, X.; Fei, C.; Lv, L.; Cao, G. Enhanced Performance of PbS-quantum-dot-sensitized Solar Cells via Optimizing Precursor Solution and Electrolytes. Scientific Reports 2016, 6 (1), 23094.

(36) Ko, D.-K.; Maurano, A.; Suh, S. K.; Kim, D.; Hwang, G. W.; Grossman, J. C.; Bulović, V.; Bawendi, M. G. Photovoltaic Performance of PbS Quantum Dots Treated with Metal Salts. ACS Nano 2016, 10 (3), 3382-3388.

(37) Liu, M.; Voznyy, O.; Sabatini, R.; García de Arquer, F. P.; Munir, R.; Balawi, Ahmed H.; Lan, X.; Fan, F.; Walters, G.; Kirmani, Ahmad R.; et al. Hybrid organic–inorganic inks

flatten the energy landscape in colloidal quantum dot solids. Nature Materials 2017, 16 (2), 258-263.

(38) Chuang, C.-H. M.; Brown, P. R.; Bulović, V.; Bawendi, M. G. Improved performance and stability in quantum dot solar cells through band alignment engineering. Nature Materials 2014, 13 (8), 796-801.

(39) Weidman, M. C.; Beck, M. E.; Hoffman, R. S.; Prins, F.; Tisdale, W. A. Monodisperse, Air-Stable PbS Nanocrystals via Precursor Stoichiometry Control. ACS Nano 2014, 8 (6), 6363-6371.

(40) Cao, Y.; Stavrinadis, A.; Lasanta, T.; So, D.; Konstantatos, G. The role of surface passivation for efficient and photostable PbS quantum dot solar cells. Nature Energy 2016, 1 (4), 16035.

(41) Liu, Y.; Kim, D.; Morris, O. P.; Zhitomirsky, D.; Grossman, J. C. Origins of the Stokes Shift in PbS Quantum Dots: Impact of Polydispersity, Ligands, and Defects. ACS Nano 2018, 12 (3), 2838-2845.

(42) Perdew, J. P. Density Functional Theory and the Band Gap Problem. Int. J. Quantum Chem. 2009, 28 (S19), 497–523.

(43) Kuisma, M.; Ojanen, J.; Enkovaara, J.; Rantala, T. T. Kohn-Sham Potential with Discontinuity for Band Gap Materials. Phys. Rev. B 2010, 82 (11), 115106.

(44) Greenham, N. C.; Peng, X.; Alivisatos, A. P. Charge separation and transport in conjugated-polymer/semiconductor-nanocrystal composites studied by photoluminescence quenching and photoconductivity. Physical Review B 1996, 54 (24), 17628-17637.

(45) Koole, R.; Liljeroth, P.; de Mello Donegá, C.; Vanmaekelbergh, D.; Meijerink, A. Electronic Coupling and Exciton Energy Transfer in CdTe Quantum-Dot Molecules. Journal of the American Chemical Society 2006, 128 (32), 10436-10441.

(46) Bai, G.; Zou, Y.; Li, Y.; Cai, L.; Chen, B.; Zang, J.; Hong, Z.; Chen, J.; Chen, Z.; Duhm, S.; et al. Revealing a Zinc Oxide/Perovskite Luminescence Quenching Mechanism Targeting Low-Roll-off Light-Emitting Diodes. The Journal of Physical Chemistry Letters 2022, 13 (13), 3121-3129.

(47) Habisreutinger, S. N.; Wenger, B.; Snaith, H. J.; Nicholas, R. J. Dopant-Free Planar n–i–p Perovskite Solar Cells with Steady-State Efficiencies Exceeding 18%. ACS Energy Letters 2017, 2 (3), 622-628.

(48) Noel, N. K.; Habisreutinger, S. N.; Wenger, B.; Klug, M. T.; Hörantner, M. T.; Johnston, M. B.; Nicholas, R. J.; Moore, D. T.; Snaith, H. J. A low viscosity, low boiling point, clean solvent system for the rapid crystallisation of highly specular perovskite films. Energy & Environmental Science 2017, 10 (1), 145-152.

(49) Stranks, S. D.; Eperon, G. E.; Grancini, G.; Menelaou, C.; Alcocer, M. J. P.; Leijtens, T.; Herz, L. M.; Petrozza, A.; Snaith, H. J. Electron-Hole Diffusion Lengths Exceeding 1 Micrometer in an Organometal Trihalide Perovskite Absorber. Science 2013, 342 (6156), 341-344.

(50) Speirs, M. J.; Dirin, D. N.; Abdu-Aguye, M.; Balazs, D. M.; Kovalenko, M. V.; Loi, M. A. Temperature dependent behaviour of lead sulfide quantum dot solar cells and films. Energy & Environmental Science 2016, 9 (9), 2916-2924.

(51) Bozyigit, D.; Lin, W. M. M.; Yazdani, N.; Yarema, O.; Wood, V. A quantitative model for charge carrier transport, trapping and recombination in nanocrystal-based solar cells. Nature Communications 2015, 6 (1), 6180.

(52) Clifford, J. P.; Johnston, K. W.; Levina, L.; Sargent, E. H. Schottky barriers to colloidal quantum dot films. Applied Physics Letters 2007, 91 (25), 253117.

(53) Sze, S. M.; Ng, K. K. Physics of Semiconductor Devices; Wiley, 2006.

(54) Werner, J. H. Schottky barrier and pn-junctionI/V plots — Small signal evaluation. Applied Physics A 1988, 47 (3), 291-300.

(55) Chuang, C.-H. M.; Maurano, A.; Brandt, R. E.; Hwang, G. W.; Jean, J.; Buonassisi, T.; Bulović, V.; Bawendi, M. G. Open-Circuit Voltage Deficit, Radiative Sub-Bandgap States, and Prospects in Quantum Dot Solar Cells. Nano Letters 2015, 15 (5), 3286-3294.

(56) In the equations, I_0 is the saturation current density, I_{cor} is the corrected current after subtracting the shunt current, q is the electronic charge, V is the potential drop across the junction, n is the ideality factor, k_B is Boltzmann's constant, and T is the temperature. The n values reported here are average values from the two approaches (see further details in the supporting information SIII).

Author contributions

B.H. conceived the experiments and led the project. B.H. performed material synthesis, device fabrication, characterization and F.C.M performed the DFT simulations. Y.J.C., J. H., S.Y.P., Y.W.L., and B.S.K. contribute to device optimisation and performed the PV characterization and analysis. J.T.F., J.C.Z., J.W.L., and B.H. contribute the initial DFT simulations. J.C.L. performed the time-resolved PL analysis and data fitting. J.B.P. performed the UPS analysis. S.M. contributed to the interpretation of the data and commented on the manuscript. J.I.S., S.N.C., and J.M.K. contributed to scientific discussion and provided experimental guidance.

Acknowledgements

B.H. and F.C.M acknowledge fruitful discussions with Dr. Yun Liu, Cavendish Laboratory, Cambridge. This work used resources provided by the Cambridge Tier-2 system operated by the University of Cambridge Research Computing Service (http://www.hpc.cam.ac.uk) funded by Physical Sciences Research Council (EPSRC) Tier-2 capital grant EP/P020259/1. B. H. acknowledges the financial support from the EPSRC SWIMS (EP/V039717/1) and Royal Society (RGS\R1\221009 and IEC\NSFC\211201). This work was also supported by the National Research Foundation (NRF) of Korea (2022M3H4A1A02076956).

TOC